# WAKE VORTEX SIMULATIONS USING A PARALLEL HIGH-ORDER ACCURATE NAVIER-STOKES SOLVER

**R. Steijl , H.W.M. Hoeijmakers**
**Department of Mechanical Engineering**
**University of Twente**
**Enschede, The Netherlands**

**Keywords:** *wake vortices, high-order accurate discretization, parallel computing*

## Abstract

*A well-known problem in the operation of commercial jet transports is the so-called 'wake vortex hazard'. This problem originates from the compact, strong vortices emanating from the wing tips which persist without much decay in their strength. The velocity field induced by these tip vortices forms a threat to following aircraft. Vortex wakes generally develop 3D instabilities of which the long-wavelength, or Crow [2], instability can often be observed as sinusoidal perturbations in aircraft contrails. The present paper describes a high-resolution algorithm for solving the Navier-Stokes equations developed to numerically simulate these wake-vortex flows. Results obtained for an evolving long-wavelength instability in a vortex pair are discussed.*

## 1 Introduction

The dynamics of a pair of counter-rotating initially rectilinear vortices poses an interesting problem due to the complexity of the resulting flow field and the practical relevance for aircraft operation. Air traffic control (ATC) employs a system of empirically determined separation distances between aircraft in air corridors and near airports. These separation distances form the *matrix of separations* giving the minimum separation distance as a function of the weights of the leading and the following aircraft. A number of these *matrix* elements prescribing the separation distance are the result of the hazard caused by the vortex wake. The time needed for sufficient decay or dispersal of the wake vortices of the leading aircraft to ensure a safe flight condition for the following aircraft sets the minimum separation distance that needs to be maintained. Uncertainties in navigation, radar tracking, etc. determine the other distances.

The dynamics of the aircraft vortex wake is largely determined by 3D instabilities that occur in the vortex system. The occurrence and characteristics of the instabilities are strongly influenced by atmospheric conditions such as ambient turbulence and stratification.

Ideally, the separation distances would be the absolute minimum for the specific conditions along the corridor or near the airport. Since this is not practical, the *matrix of separations* is constant and as a result conservative. A better understanding of the dynamics of aircraft vortex wakes at the actual atmospheric conditions could lead to more economical separations. Wake vortex studies could in addition be used in the development of on-board devices that can modify and control the wake decay and dispersal.

Since the early 1990s the effort devoted to wake vortex research has increased significantly as a result of the ever increasing traffic densities around large airports and in corridors. In addition, the forthcoming introduction of a new generation of very large passenger aircraft stimulated this research.

Wake vortices decay under the influence of:

- molecular viscosity,
- turbulence, when the vortex pair traverses a turbulent atmosphere,
- 3D cooperative instabilities.

The cooperative instabilities are a result of the mutually induced velocity of the vortices forming the vortex pair and can be divided in two categories:

- long-wavelength (Crow [2]) instability, with a wavelength of the order 5 to 10 times the initial spacing of the vortex pair,
- short-wavelength (*elliptic*) instability, which has a wavelength comparable to the vortex core size.

  Recently, this type of instability was clearly visualized in a water-tank experiment by Leweke et al. [7].

A review of recent wake vortex research is given by Spalart [11]. In the last few years, both direct numerical simulations (DNS) and large eddy simulations (LES) have been performed by a number of research teams to study certain aspects of the problem. The influence of atmospheric turbulence on the decay of wake vortex pairs, for example, has been studied by Riso et al. [9], Proctor and co-workers [4] and others. Various vortex decay models have been introduced by Sarpkaya [10] predicting the descent and decay of aircraft trailing vortices subjected to realistic environmental conditions. Recently this model was compared to data obtained with Lidar in experiments carried out in the 1990s at Memphis and Dallas-Fort Worth airports. Sarpkaya [10] showed that field data and predictions compare reasonably well.

However, observed behaviour for some flights cannot be explained by computations nor by decay models similar to [10]. Therefore, further research is needed to understand more of the dynamics of aircraft wake vortex pairs.

The present research aims at studying details of the dynamics of the 3D instabilities (both long-wavelength and short-wavelength) that enhance the decay of the vortex pair. For this purpose, a high-order accurate Navier-Stokes solver has been developed that enables time-accurate simulations of 3D flows on multi-processor computers (both high-end supercomputers and affordable workstations). The present paper shows results for a model vortex pair in an unstratified, quiescent medium.

This paper gives a description of the numerical method used for these simulations and presents and discusses results of the method.

## 2 Numerical method

The present numerical method was designed for parallel high-resolution simulations of three-dimensional flows. Given the simplicity of the computational domains in the envisaged applications, a spectral method ([1], [3]) could have been chosen. However, flexibility of boundary conditions is limited for these methods. This flexibility is necessary in, for example, simulations of the interaction of vortex systems with solid walls. Non-periodic formulations in the direction normal to that boundary are required. Therefore, for the numerical method in the present research, high-order accurate compact-difference discretizations ([6], [12]) were chosen. Such discretizations can be formulated for very general coordinate systems and complex geometries, as is shown in Visbal et al. [13]. To enhance numerical stability, a high-order compact-difference filtering is generally used in conjunction with compact-difference discretizations of the Navier-Stokes equations. The low-pass filters used have a truncation error that is of higher order than the spatial discretization error and eliminates the poorly resolved Fourier modes.

### 2.1 Governing equations

The Navier-Stokes equations for an incompressible Newtonian medium with constant viscosity in Cartesian coordinates to be discretized are:

$$\frac{\partial \mathbf{w}}{\partial t} + u\frac{\partial \mathbf{w}}{\partial x} + v\frac{\partial \mathbf{w}}{\partial y} + w\frac{\partial \mathbf{w}}{\partial z} = -\frac{1}{\rho}\nabla p + \nu\Delta\mathbf{w} \quad (1)$$

$$\nabla \cdot \mathbf{w} = 0 \quad (2)$$

In equation (1), $\mathbf{w}$ is the velocity vector, $p$ is the pressure, $\rho$ the (constant) density and $\nu$ the kinematic viscosity of the medium. Relation (2) is the divergence-free constraint on the velocity field, as a result of the incompressibility of the medium. The fractional time-stepping method of Kim & Moin [5] is used in the present simulation method. The time-stepping method is second-order accurate in time and consists of 3 steps. The first step applies the explicit Adams-Bashfort method to the nonlinear convection terms and the implicit Crank-Nicholson scheme to the viscous terms. This results in 3 independent Helmholtz equations for the updated velocity components:

$$\left(1-\frac{\Delta t}{2Re}\nabla^2\right)v_i = -\Delta t\left(\frac{3}{2}H_i{}^n-\frac{1}{2}H_i{}^{n-1}\right) + \left(1+\frac{\Delta t}{2Re}\nabla^2\right)w_i^n \qquad (3)$$

with $H_i$ the nonlinear convection terms in skew-symmetric form:

$$H_i=\frac{1}{2}\left[\frac{\partial w_i w_j}{\partial x_j}+w_j\frac{\partial w_i}{\partial x_j}\right] \qquad (4)$$

In equation (3), $n$ denotes the last completed time-step, $v_i$, the velocity vector at an intermediate step between $n$ and $n+1$. The next step is the solution of a Poisson equation for a modified pressure $\phi$, linked to the pressure as: $p=\phi-(\Delta t/2Re)\nabla^2\phi$,

$$\nabla^2\phi=\frac{1}{\Delta t}\frac{\partial v_i}{\partial x_i} \qquad (5)$$

A time-step is completed with

$$w_i{}^{n+1}=v_i-\Delta t\frac{\partial\phi}{\partial x_i} \qquad (6)$$

## 2.2 Spatial discretization

First derivatives are discretized using compact-difference expressions of sixth-order accuracy given by Lele [6]. Equations (3) and (5) are discretized using a three-dimensional compact-difference operator shown in Steijl & Hoeijmakers [12].

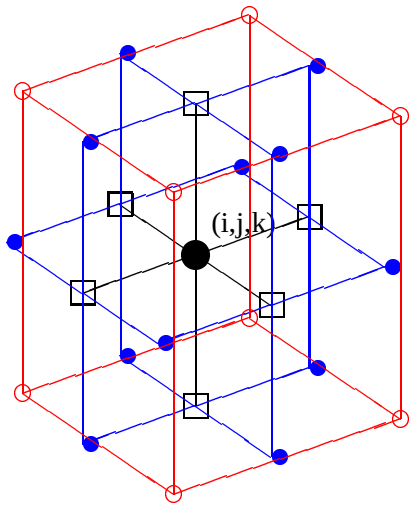


**Fig. 1** Stencil of compact-difference Laplace operator around node $(i,j,k)$.

The formulation uses a 27-point stencil around the mesh point $(i,j,k)$. This stencil is shown in Fig. 1 with the 6 nodes $(i\pm1,j,k),(i,j\pm1,k),(i,j,k\pm1)$ depicted as □, the 12 nodes $(i\pm1,j\pm1,k),(i,j\pm1,k\pm1),(i\pm1,j,k\pm1)$ shown as ● and the 8 vertices $(i\pm1,j\pm1,k\pm1)$ as ○. The Helmholtz/Poisson equations (3), (5) can be written in a generic way as:

$$-\Delta f+\lambda f=R \qquad (7)$$

This equation is discretized as:

$$\begin{aligned}&\frac{1}{h^2}\Big[\left(8(1-\beta)+\frac{12+\lambda h^2}{6}\lambda h^2\right)f(i,j,k)\\&-\left(\frac{2}{3}-4\beta\right)[f(i\pm1,j,k)+f(i,j\pm1,k)+\\&\qquad f(i,j,k\pm1)]\\&-\left(\frac{1}{3}+2\beta\right)[f(i\pm1,j\pm1,k)+\\&\quad f(i\pm1,j,k\pm1)+f(i,j\pm1,k\pm1)]\\&+\beta f(i\pm1,j\pm1,k\pm1)\Big]\\&=2R+\frac{h^2}{6}\Big[\Delta R+\lambda R\Big]+O(h^4)\end{aligned} \qquad (8)$$

Parameter $\beta$ can be used to eliminate one of the groups of elements from the stencil in Fig. 1 and/or specify certain conditions on the resolving properties in Fourier space.

### 2.3 Solution procedure

Applying expression (8) to the discretization of the Helmholtz equations for the updated velocity components, equation (3), and the Poisson equation for the pressure, equation (5), results in sparse-matrix systems of linear equations. In a parallel simulation, the Navier-Stokes equation (1) and (2) are solved in each of the sub-domains that result from the decomposition of the computational domain in sub-domains. For each sub-domain, the number of equations is identical to the number of nodes used in the discretization. The maximum number of non-zero elements per row (each equation corresponds to one row of the sparse-matrix system) is 27, the number of elements in the stencil on the left-hand side of expression (8). The systems of equations are solved using the Preconditioned Conjugate Gradient method in case the matrix is symmetric. Neumann boundary conditions lead to an non-symmetric sparse-matrix to which the Preconditioned Bi-Conjugate Gradient is applied.

To optimize numerical performance of these Krylov solvers, sparse-storage formulations ([8]) are not used. Instead, the regularity of the computational domain is used to formulate the matrix-vector multiplications in the (Bi-)Conjugate Gradient method in terms of a system of multiple loops.

## 3 Numerical results

### 3.1 Evolving Crow instability

A developing long-wavelength instability in a pair of trailing vortices is considered within a cubic computational domain. A general impression of the test case can be obtained from Fig. 4, showing the vortex pair at five different instances in time. Here, $T$ is the time non-dimensionalized by $\frac{\Gamma}{2\pi b_0^2}$. The 2 vortices are initially straight line-vortices separated by distance $b_0$. Periodicity is assumed in $x$-direction. This assumption is justified by the sinusoidal perturbations predicted by the theories of both Crow [2] and Widnall et al. [14]. The computational domain is divided in 4 sub-domains in the periodic direction in order to carry out the parallel simulations. The azimuthal velocity of both vortices has a Gaussian profile in the cores of radius $r_c$. In Cartesian coordinates, the induced velocity of each of the rectilinear vortices is of the form:

$$\begin{aligned} u(x,y,z) &= 0 \\ v(x,y,z) &= \frac{(z-z_c)\Gamma}{2\pi}\frac{\left[1-\exp(-\alpha r^2/r_c^2)\right]}{r^2} \\ w(x,y,z) &= -\frac{(y-y_c)\Gamma}{2\pi}\frac{\left[1-\exp(-\alpha r^2/r_c^2)\right]}{r^2} \end{aligned} \qquad (9)$$

with $r^2 = (y-y_c)^2 + (z-z_c)^2$, where the vortex center is located in $(y_c, z_c)$. The constant $\alpha$ in the exponent is chosen to position the maximum of the azimuthal velocity at $r_c$ (this leads to the constraint $(2\alpha+1)e^{-\alpha} = 1$).

For an isolated vortex with this velocity distribution theory gives for the growth of the core radius $r_c$ and for the decay of the maximum of the azimuthal velocity $u_{\theta,max}$:

$$\begin{aligned} r_c(t) &\sim \sqrt{t} \\ u_{\theta,max} &\sim 1/\sqrt{t} \end{aligned} \qquad (10)$$

Fig. 2 shows the distribution of the initial induced vertical velocity component of the closely spaced vortex pair along a horizontal line through both vortex cores. It is shown in the figure that 81 mesh points in $y$ direction (the horizontal cross-flow direction) is adequate to resolve the initial velocity field.

The vortex centers are located at $y = 0.875$ and $y = 1.125$, at which locations a significant down-wash is present due to the mutual induction of the vortices. To prevent the vortices from advecting out of the computational domain during the simulation, a constant vertical velocity equal to the theoretical sink rate of the vortices is superposed on the initial velocity field. This has an effect similar to using a frame of reference that moves at constant speed.

Fig. 3 shows the initial vorticity distribution (the component of the vorticity vector in $x$-direction) along this line.

The pressure field for an isolated vortex can be found by integration of

$$\frac{\partial p}{\partial r} = \rho\frac{u_\theta^2}{r} \qquad (11)$$

with $r$ the distance from the vortex core. However, for the more complex flow field of the closely-spaced vortex pair the pressure field is more easily computed using the flow solver employing a small number of very small time-steps. For the present azimuthal velocity profile

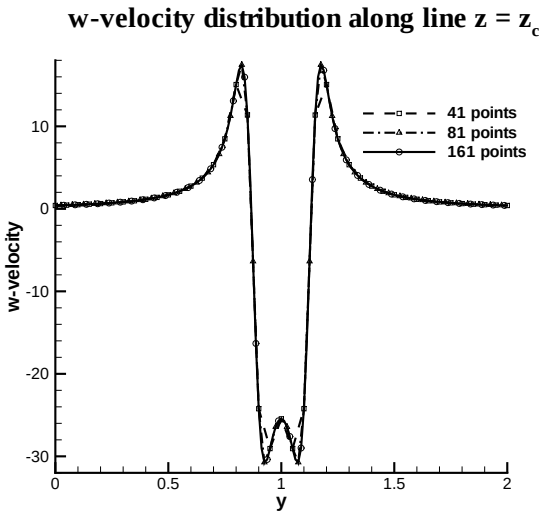


**Fig. 2** W-component of velocity along horizontal line through both vortex cores in case of unperturbed vortices ($T = 0$).

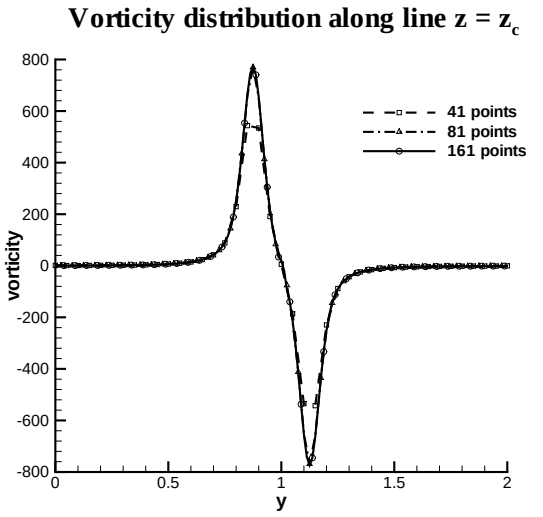


**Fig. 3** Vorticity distribution along horizontal line through both vortex cores in case of unperturbed vortices ($T = 0$).

(Lamb-Oseen) and $r_c/b_0 = 0.2$, both the theory of Crow [2] and Widnall et al. [14] give as wavelength $\lambda$ for the most unstable mode: $\lambda/b_0 = 8$. This wavelength determines the dimension of the computational domain in $x$-direction: one long-wavelength instability mode is initialized in the initial solution. This initial mode is given an amplitude $\delta/r_c = 0.25$. Table (1) shows some characteristic parameters for this test case.

All simulations were performed using a cubic computational domain of dimension 2.0m in each direction. A division in 4 sub-domain was used in the $x$-direction that enabled parallel computations on 4 CPUs. Three simulations are discussed in this study: the base-line simulation at a Reynolds number of $6.7 \times 10^5$ on a $81^3$ mesh and two variations. Varied are the Reynolds number, i.e. a reduction to $6.7 \times 10^3$ and the mesh resolution, i.e. an increased resolution of $121^3$. The Reynolds number is reduced from $6.7 \times 10^5$ to $6.7 \times 10^3$ as a result of a factor 100 increase in kinematic viscosity.

**Table 1** Parameters for evolving Crow instability test case

| Test case: | Low Re coarse | High Re coarse | High Re fine |
|---|---|---|---|
| $\mathrm{Re}(\Gamma_0/\nu)$ | $6.7 \times 10^3$ | $6.7 \times 10^5$ | $6.7 \times 10^5$ |
| $\Gamma_0$ $[m^2/s]$ | 10.0 | 10.0 | 10.0 |
| Mesh | $81^3$ | $81^3$ | $121^3$ |
| nodes | $6.0 \times 10^5$ | $6.0 \times 10^5$ | $1.9 \times 10^6$ |
| Mem.[Mb] | 148 | 148 | 384 |
| $r_c/b_0$ | 0.2 | 0.2 | 0.2 |
| $\lambda/b_0$ | 8.0 | 8.0 | 8.0 |

## 3.2 Discussion

Fig. 4 shows a three-dimensional view of the growth most unstable Crow instability mode between T=1.27 and T=3.82. Since periodic boundary conditions are prescribed in $x$-direction, the computational domain is sized to contain just one instability mode. Fig. 4 shows two modes for clarity. These are the results for the low-

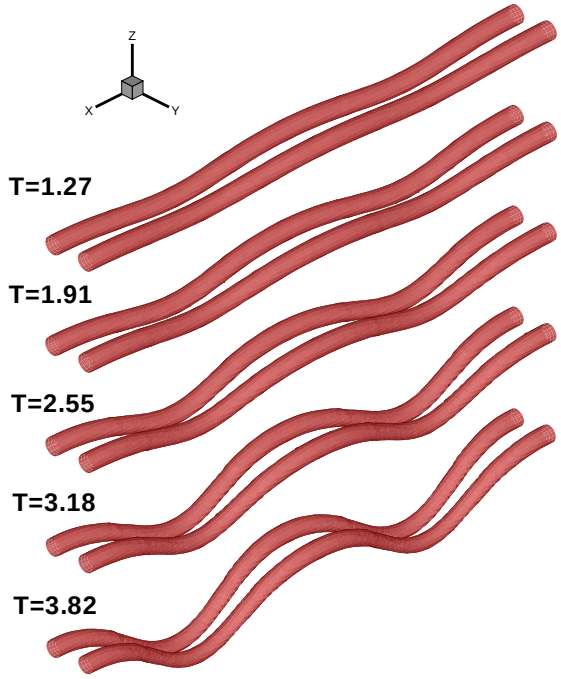


**Fig. 4** Growth of Crow instability between T=1.27 and T=3.82. Iso-pressure contour (p=101000 Pa). Simulation on $81^3$ mesh, Reynolds number $6.7 \times 10^3$.

Reynolds number simulation on the $81^3$ mesh. A rapid growth occurs for the sinusoidal perturbation. The amplitude of the sinusoidal perturbation is presented in Fig. 5 for both Reynolds numbers, both for a linear and a logarithmic scale. A comparison is made with the inviscid asymptotic theory of Widnall. For $T < 2.5$ the growth is exponential in both simulations. A good agreement with the asymptotic theory is obtained. At later times, the growth rate is reduced in comparison with the results of the asymptotic theory. This can be attributed to both the reduction of circulation and the increasing radii of vortex cores as a result of the viscous decay. For the lower Reynolds number simulation this effect is stronger due to the larger kinematic viscosity.

The effect of mesh resolution is shown in Fig. 6, where the growth of the perturbation for small $T$ for the high Reynolds number simulations on the $81^3$ and $121^3$ meshes is compared. It can be seen that the coarse-mesh and fine-mesh results are very similar, the result for the $121^3$ mesh being slightly closer to the result from the asymptotic theory. From this figure it can be concluded that the $81^3$ mesh results in an adequate resolution of the flow field.

Fig. 7 and Fig. 8 show a sequence of pictures at different times between T=1.27 and T=3.50 for both Reynolds numbers. On the left, a top view of the computational domain is shown. The side view is shown on the right. At later times, the vortices start a reconnection process that is clearly visible from the top-view figures. Results presented on the $81^3$ mesh in both cases.

## 4 Conclusion

A high-order accurate numerical method has been developed that is used in this paper for time-dependent three-dimensional Navier-Stokes simulations of an evolving long-wavelength instability in a trailing vortex pair. The results show a good resolution of the flow field using a $81^3$ mesh. The required resources for a simulation on a mesh of this size are modest with respect to the memory needed. For the limited number of CPUs used in the present study (4), the CPU times are acceptable. For the coarse-mesh simulations, a run-time of 18 hours on 4 CPUs (SGI R10K) was required for 1000 time-steps. Future work will include simulations of physically more complex flows, such as test cases with interactions of long-wavelength and short-wavelength instabilities.

## References

[1] Canuto C, Hussaini M, Quarteroni A, and Zang T. *Spectral methods in fluid dynamics.* 1st edition, Springer Verlag, 1987.

[2] Crow S. Theory for a pair of trailing vortices. *AIAA Journal*, Vol. 8, No 12, pp 2172–2179, 1970.

[3] Gottlieb D and Orszag S. *Numerical analysis of spectral methods.* 1st edition, SIAM, Philadelphia, 1977.

[4] Han J, Lin Y.-L, Schowalter D, Arya S. P, and Proctor F. Large eddy simulations of aircraft wake vortices within homogeneous turbulence:

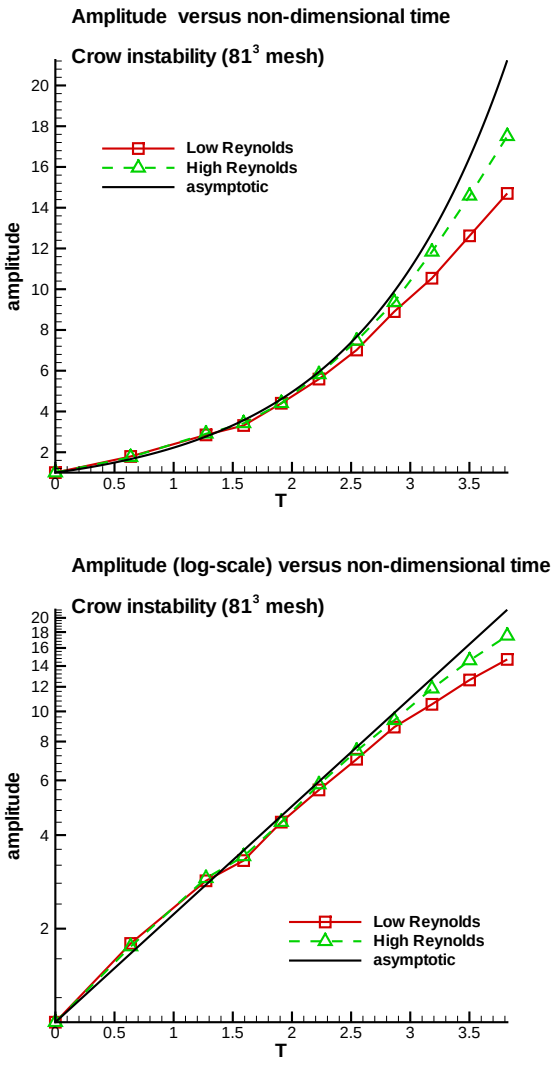


**Fig. 5** Growth of Crow instability mode for Reynolds number $6.7 \times 10^3$ and $6.7 \times 10^5$. Coarse mesh ($81^3$). Linear scale (top) and log-scale (bottom).

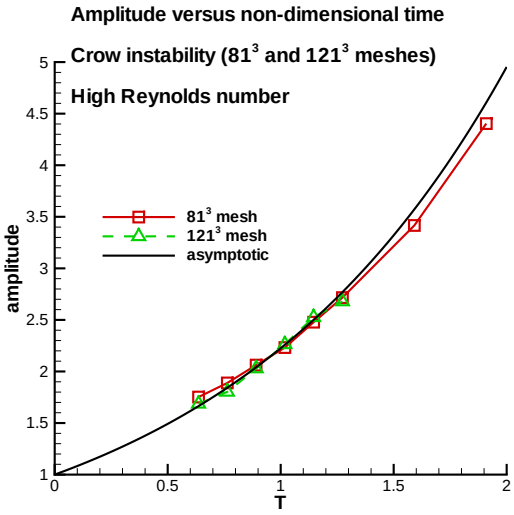


**Fig. 6** Growth of Crow instability mode for Reynolds number $6.7 \times 10^5$. Coarse mesh ($81^3$) and fine mesh ($121^3$).

Crow instability. *AIAA Journal*, Vol. 38, No 2, pp 292–300, 2000.

[5] Kim J and Moin P. The structure of the vorticity field in turbulent channel flow. *Journal of Fluid Mechanics*, Vol. 162, pp 339–363, 1986.

[6] Lele S. Compact finite difference schemes with spectral-like resolution. *Journal of Computational Physics*, Vol. 103, pp 16–42, 1992.

[7] Leweke T and Williamson C. Cooperative elliptic instability of a vortex pair. *Journal of Fluid Mechanics*, Vol. 360, pp 85–119, 1998.

[8] Press W, Teukolsky S, Vetterling W, and Flannery B. *Numerical Recipes in C: The Art of Scientific Computing.* 2nd edition, Cambridge University Press, 1994.

[9] Risso F, Corjon A, and Stoessel A. Direct numerical simulations of wake vortices in intense homogeneous turbulence. *AIAA Journal*, Vol. 35, pp 1030–1040, 1997.

[10] Sarpkaya T. A new model for vortex decay in the atmosphere. *Journal of Aircraft*, Vol. 37, No 1, pp 53–61, 2000.

[11] Spalart P. Airplane trailing vortices. *Ann. Rev. Fluid Mech.*, Vol. 35, pp 107–138, 1998.

[12] Steijl R and Hoeijmakers H. A high-order accurate compact finite difference algorithm for the incompressible navier-stokes equations. *Proc Second AFOSR International Conference on DNS/LES.*, pp 385–396, New Brunswick, NJ, June 7-9, 1999.

[13] Visbal M and Gaitonde D. High-order accurate method for unsteady vortical flows on curvilinear meshes. *AIAA 98-0131*, 1998.

[14] Widnall S. E, Bliss D, and Zalay A. Theoretical and experimental study of the stability of a vortex pair. *Proc Aircraft wake turbulence and its detection.*, pp 305–338, Seattle, WA, September 1-3, 1970.

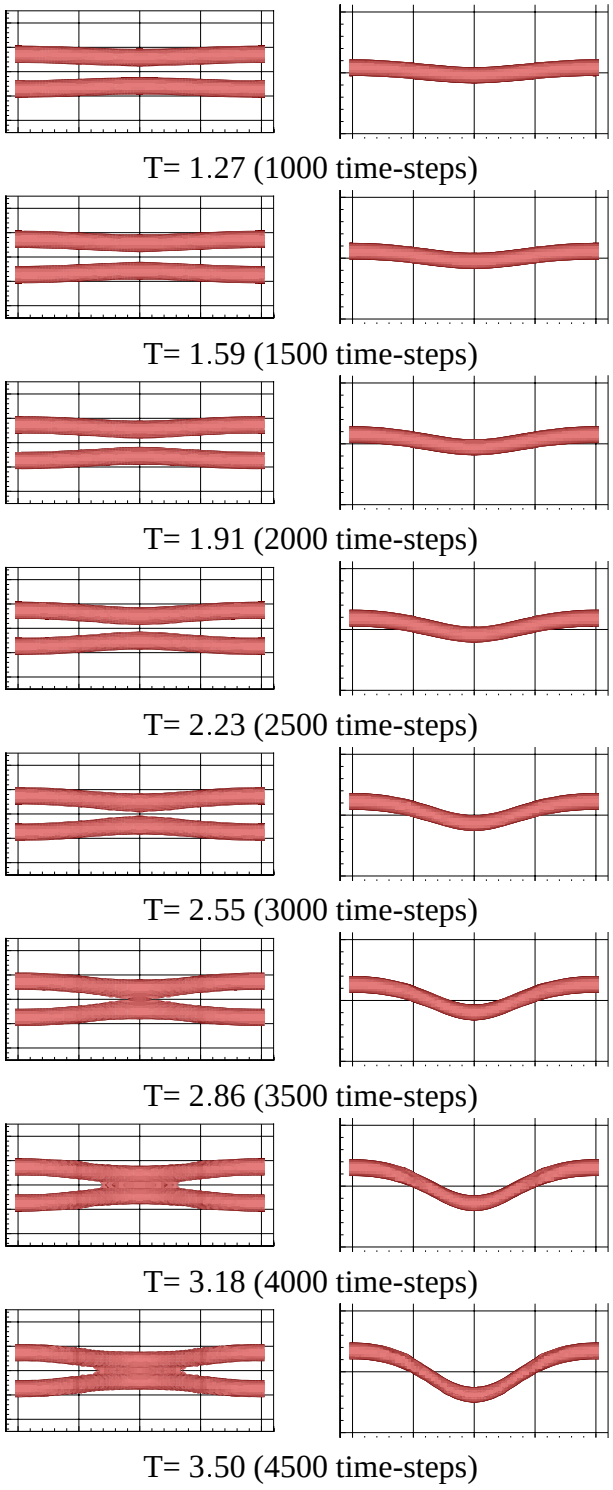


**Fig. 7** Iso-pressure contour (p=101000 Pa). High Reynolds number. Simulation on $81^3$ mesh.

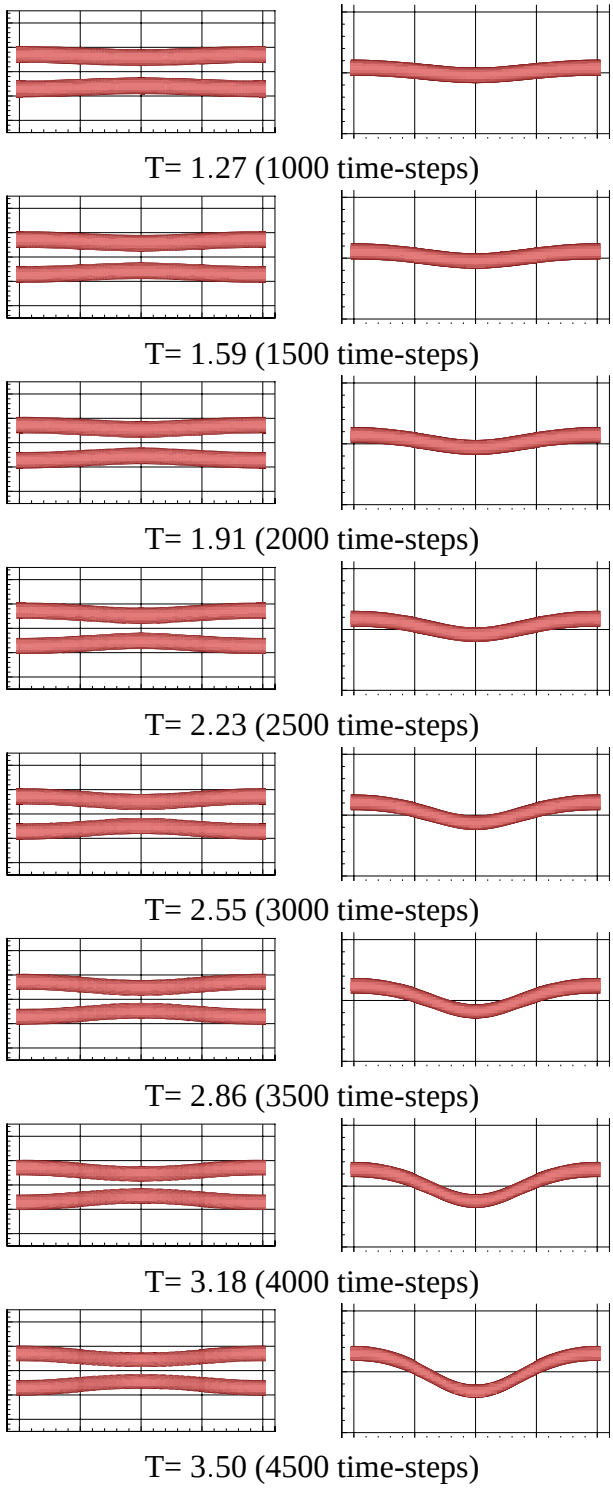


**Fig. 8** Iso-pressure contour (p=101000 Pa). Low Reynolds number. Simulation on $81^3$ mesh.